ELSEVIER

Journal of Alloys and Compounds 320 (2001) 177–188

Journal of ALLOYS AND COMPOUNDS

www.elsevier.com/locate/jallcom

The compound energy formalism: applications

Karin Frisk[a,*], Malin Selleby[b]

[a]Swedish Institute for Metals Research, Drottning Kristinas väg 48, SE-114 28 Stockholm, Sweden
[b]Department of Materials Science and Engineering, Royal Institute of Technology, SE-100 44 Stockholm, Sweden

1. Introduction

The compound energy formalism was introduced 30 years ago [1] in order to describe the Gibbs energy of solution phases with sublattices. It has been developed in several steps and applied to phases of different characters. It is widely used in so-called CALPHAD assessments of binary and higher order systems. The developments of the formalism are described in an accompanying paper [2]. The present paper will give a review of various types of applications of the compound energy formalism. In the individual descriptions of the theoretical background, reference will frequently be made to the appropriate sections in the accompanying paper.

The first example illustrates the application of the compound energy formalism to an interstitial solution of nitrogen in multicomponent alloys. The following three examples illustrate the modelling of solid oxide phases. Examples 5 and 6 treat the modelling of ionic melts. With the extension of the models to multicomponent systems applications to practical problems are possible, which is illustrated in Examples 1, 6 and 7. Some aspects of the optimisation of the thermodynamic parameters involved in the models are discussed in Examples 7 and 8. Finally, the treatment of ordering using the compound energy formalism is discussed in Examples 9, 10 and 11.

2. Examples

Example 1. The solubility of N in multicomponent alloys (reference section 5 in Ref. [2]).

N is used as an alloy element in many high performance, high alloy, stainless steels since it has been found to improve mechanical properties and corrosion and wear resistance [3]. Thermodynamic modelling of the interstitial solubility of N in multicomponent alloys is thus of large practical interest. A long term work in assessing alloy systems by the CALPHAD method [4] using the compound energy formalism makes it possible today to perform reliable calculations in multicomponent systems by combining the assessments of lower order systems. Experience has shown that the predictions of phase equilibria in multicomponent systems, which can be made by this method, are sufficiently accurate for most purposes. Some examples of quantitative verification of calculated equilibria, obtained by comparison with experimental information on commercial steel compositions, can be found in Ref. [5]. Some examples of the use of thermodynamic calculations applied to N-alloyed stainless steel, and comparisons with experimental information were presented in Ref. [6]. The modelling of the solubility of N in multicomponent ferrite and austenite phases using the compound energy formalism is discussed below, and some examples of the reliability of the predicted N solubilities are given.

The description of the solubility of N in the ferrite and austenite phases in a stainless steel involves a number of alloying elements. To describe equilibria in commercial alloys a six component system is often necessary and the example below is given for the system Cr–Fe–Mn–Mo–N–Ni. The ferrite phase (bcc) is described by the model $(Fe, Cr, Mn, Mo, Ni)_1(N, Va)_3$, and the austenite phase (fcc) by the model $(Fe, Cr, Mn, Mo, Ni)_1(N, Va)_1$. The solubility of N in ferrite and austenite falls within the region of high vacancy content on the second, interstitial sublattice. The expression for the Gibbs energy following Ref. [2], section 2, is given by

$$G_m = \sum_{\mathrm{Me}} y_{\mathrm{Me}} y_{\mathrm{N}} {}^{\mathrm{o}}G_{\mathrm{Me:N}} + \sum_{\mathrm{Me}} y_{\mathrm{Me}} y_{\mathrm{Va}} {}^{\mathrm{o}}G_{\mathrm{Me:Va}} + {}^{\mathrm{E}}G_m \qquad (1)$$

The expression for the last term, the excess term, is given in Eq. (5) in Ref. [2]. The first term involves the parameter ${}^{\mathrm{o}}G_{\mathrm{Me:N}}$ which represents the Gibbs energy of a binary nitride. In the model for bcc it represents the Gibbs energy of the MeN_3 nitride and in the model for fcc it represents the Gibbs energy of the MeN nitride. This parameter should be determined from experimental or estimated information on the nitrides. The excess term can

*Corresponding author.

0925-8388/01/$ – see front matter
PII: S0925-8388(00)01482-1

be fitted to the information on the solubility of N in the bcc and fcc phases in the low N content range. In equilibrium with N_2 gas the nitrides are not always stable, but when calculating equilibria in N containing alloys without including the gas phase the nitrides may appear. In the assessment work it is important to check that the temperature and composition ranges of these nitrides are reasonable, and adjust the ${}^{o}G_{Me:N}$ parameters accordingly.

The parameters, which are involved in the expression for the Gibbs energy in the six-component system given above, can be taken from assessments of the lower order systems. In this particular case 25 full assessments of binary, ternary and quaternary systems have been performed. By combining them the solubility of N in the multicomponent alloy can be calculated. The full line in Fig. 1A shows the calculated solubility of N, as predicted from the combination of the lower order assessments, compared with a few experimental points from Ref. [7]. The experimental N content is expected to be lower than the equilibrium content for the high N activities. The dashed line in Fig. 1A shows the prediction of the N solubility from unary, binary and ternary parameters, and with all higher order parameters set to zero. The dashed curve shows that an extrapolation from ternary assessments would be very valuable in the planning of this type of experiments.

Fig. 1B shows an example of the use of thermodynamic information on N solubilities in a kinetic model calculation. The figure shows a calculation of the austenite phase fraction in three duplex stainless steels [8]. The experimental points were obtained by subjecting the steels to weld simulation treatments by a ferritizing heat treatment, cooling with a specified rate, and quenching. The calculations were performed by applying a kinetic model, and assuming that the transformation from ferrite to austenite is governed by N diffusion and that the transformed austenite inherits the metallic element content from the ferrite. The phase fractions were calculated from the kinetic model using the N contents of the phases which were calculated from the thermodynamic parameters. The only adjustable parameter used in the calculation was the nucleation rate. The agreement with the experimental information confirms that the calculated N contents of the phases are predicted with sufficient accuracy.

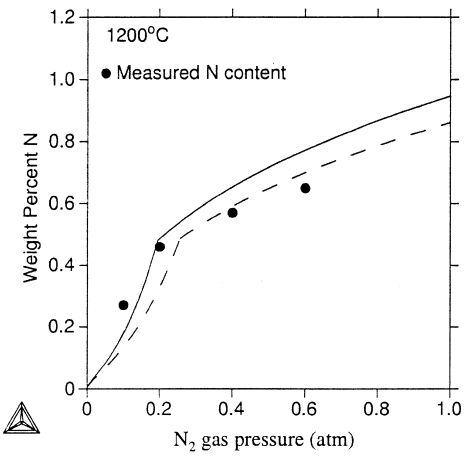

(A)

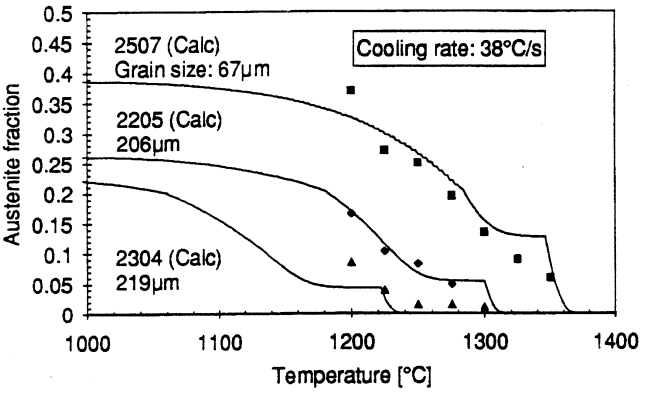

(B)

Fig. 1. (A) The calculated equilibrium N content in a Fe–19%Cr–8%Mn–6%Ni–3%Mo alloy (solid line). The calculated equilibrium N content predicted from binary and ternary assessments is shown by the dashed line. The experimental datapoints [7] show the N content measured in nitrided powders exposed to the nitrogen pressure given in the *x*-axis. (B) The calculated austenite phase fraction in three duplex stainless steels after a weld simulation treatment as a function of the quenching temperature [8]. The samples were cooled with a rate of 38 K/s from the ferritizing temperature to simulate the heat affected zone conditions in a weld. The composition of the alloys are; Alloy 2507: 24%Cr, 7%Ni, 4%Mo, 0.29%N; Alloy 2205: 22%Cr, 5.7%Ni, 3%Mo, 0.18%N; Alloy 2304: 22%Cr, 4.7%Ni, 0.12%N.

Example 2. Modelling of wüstite and lime (reference section 10 in Ref. [2]).

Wüstite, FeO, has the sodium chloride structure with oxygen ions forming a fcc lattice with iron ions on the octahedral interstitial sites. Sundman [9] modelled the phase using two sublattices, $(Fe^{+2}, Fe^{+3}, Va)_1(O^{-2})_1$. The structure can be shown in a Gibbs triangle, see Fig. 2A, since there are three compounds in the model, $(Fe^{+2})(O^{-2})$, $(Fe^{+3})(O^{-2})$ and $(Va)(O^{-2})$. The latter two have a net charge and in order to maintain electroneutrality the constitution of wüstite has to be on the line in Fig. 2A. Along that line the site fraction of vacancies is half the fraction of Fe^{+3} ions. According to the compound energy formalism [2] the molar Gibbs energy of wüstite is

$$G_m = \sum_i y_i {}^{o}G_{i:O^{-2}} + RT \sum_i y_i \ln y_i + {}^{E}G_m \qquad (2)$$

where i stands for Fe^{+2}, Fe^{+3} and neutral Va. For convenience, ${}^{o}G_{Va:O^{-2}}$ was set to zero since this quantity will occur in other systems without iron. There are three types of interaction parameters but only the interaction

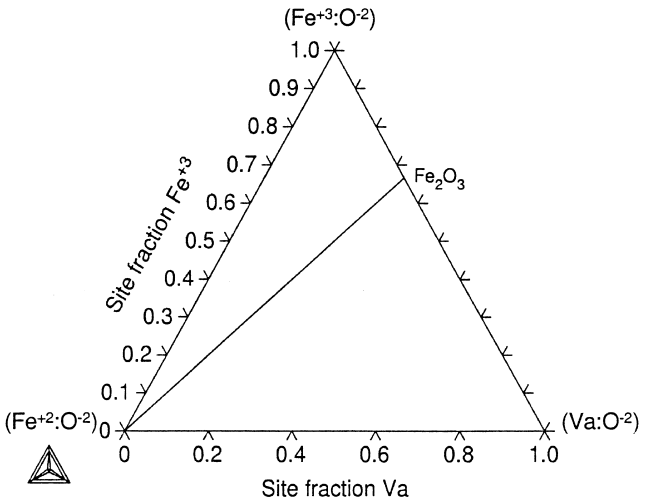

(a)

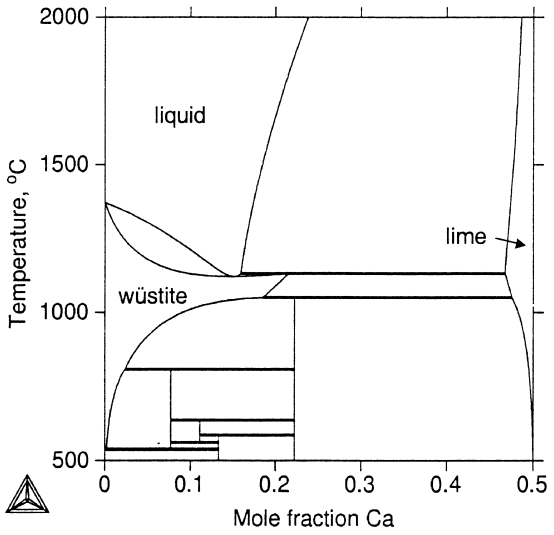

(b)

Fig. 2. (A) A Gibbs triangle showing the structure of wüstite. In order to maintain electroneutrality the constitution of wüstite has to be on the line. (B) The iron saturated section of the Ca–Fe–O system. The iron saturation gives a phase diagram close to the FeO–CaO section. There is a miscibility gap between the two sets of the halite phase, i.e. between lime and wüstite.

between Fe^{+2} and Fe^{+3} was evaluated, all the parameters with Va were set to zero.

Lime, CaO, has the same structure as stoichiometric wüstite. When the Ca–Fe–O system was evaluated [10] the mutual solubility of CaO and FeO was modelled by adding Ca^{+2} to the first sublattice. Interaction parameters between Ca^{+2} and Fe^{+2} and Fe^{+3}, respectively, were evaluated. The iron saturated section of the Ca–Fe–O system is plotted in Fig. 2B. The iron saturation gives a phase diagram close to the FeO–CaO section. Barry [11] suggested halite, from the NaCl system, as a generic name for the phase. In Fig. 2B there is a miscibility gap between the two sets of the halite phase, i.e. between lime and wüstite.

Example 3. Defect content of double oxide, Fe_2SiO_4, as function of oxygen potential (reference section 10 in Ref. [2]).

Fayalite has an ideal composition of Fe_2SiO_4 but the Fe content can decrease due to the possibility of Fe^{+2} to oxidise to Fe^{+3}. Furthermore, the Fe content can increase by Fe going into the Si sublattice. The properties of the phase were analysed by Hillert et al. [12] using a compound energy model with the formula $(Fe^{+2}, Fe^{+3}, Va^0)_2(Si^{+4}, Fe^{+3})_1(O^{-2})_4$. The three defects in this formula were taken from a proposal by Nakamura and Schmalzried [13]. Due to electroneutrality there are only two degrees of freedom. Nakamura and Schmalzried could thus define the deviation from the ideal composition with two independent variables, which they chose as follows:

$$\xi = N_{Si}/(N_{Si} + N_{Fe}) - 1/3 \quad (3)$$

$$\eta = N_O/(N_{Si} + N_{Fe}) - 4/3 \quad (4)$$

Using a dilute solution model they predicted that the second variable should vary with the oxygen pressure as

$$\eta = K(P_{O_2})^{1/n} \quad (5)$$

with $n = 5.5$ but their data seemed to indicate $n = 5$. They explained this by proposing that there is a strong association between Fe^{+3} on the Fe sublattice and on the Si sublattice. They were thus able to derive an equation yielding $n = 5$. However, in their computer-assisted optimisation using the compound energy formalism, Hillert et al. were able to represent the data very well without taking the association into account, which could have been done with the compound energy formalism by artificially giving the Fe ions on the Si sublattice a valency of $+4$. That would yield the same equation that Nakamura and Schmalzried derived.

With the compound energy formalism there are six compound energies. They will here be denoted by abbreviating Fe^{+2} as 2, Fe^{+3} as 3 and Si^{+4} as S. The experimental data were confined to $\xi = 0$ and allowed only two independent parameters to be evaluated. The quantity for the ideal composition, $\Delta_f{}^oG_{2:S}$, was known from a previous assessment of the whole Fe–Si–O system. All the other compounds are charged and $\Delta_f{}^oG_{2:3}$ was put to zero in order to be a reference for charges. Of the remaining five, those two that are formed by combining two defects were given relative to the other ones, assuming that the Gibbs energy for two reciprocal reactions are zero.

$$\Delta_f{}^oG_{3:3} = \Delta_f{}^oG_{2:3} + \Delta_f{}^oG_{3:S} - \Delta_f{}^oG_{2:S} \quad (6)$$

$$\Delta_f G_{V:3} = \Delta_f{}^oG_{2:3} + \Delta_f{}^oG_{V:S} - \Delta_f{}^oG_{2:S} \quad (7)$$

The two optimisation parameters were thus $\Delta_f{}^oG_{3:S}$ and $\Delta_f{}^oG_{V:S}$ and they represent the Gibbs energy of formation of Fe^{+3} and Va^0, respectively, on the Fe sublattice.

In the Fe–Si–O system at 1403 K the fayalite phase takes part in two-phase equilibria with Fe_3O_4, wüstite, metallic iron and SiO_2, respectively. Fig. 3A shows the calculated deviations from the ideal composition around its field of existence. It is interesting to note that experimental information was limited to the dotted line. It was obtained by varying the oxygen pressure for a specimen with close to the ideal Fe/Si ratio, i.e. $\xi = 0$. The horizontal width of the fayalite phase field is thus a result of the thermodynamic analysis and depends to a large extent on how the thermodynamic properties of the other phases have been determined.

The oxygen pressure has an effect on all three kinds of defects and the calculated effect on the vacancies in the Fe sublattice and of Fe^{+3} in the Si sublattice is shown in Fig. 3B. Again the dotted lines show the variations for a specimen with a close to ideal Fe/Si ratio. The upper one is for y'_{Va} and the lower one for y''_{Fe+3}.

Example 4. Deficit and excess of oxygen in double oxide, $MgO–Al_2O_3$ (reference section 10 in Ref. [2]).

An excess of oxygen in an oxide can be modelled by introducing vacancies in the sites for metal atoms. An oxygen deficit can be modelled by introducing vacancies in the oxygen sites but also by introducing metal atoms in a new sublattice, an interstitial one which would be empty in the ideal case. The latter alternative applies to spinel, the intermediate phase in the $MgO–Al_2O_3$ system. In addition, there are defects allowing a large variation in the Al/Mg ratio in both directions from the ideal value.

The $MgO–Al_2O_3$ system was analysed by Hallstedt [14] using a compound energy model based on the formula $(\mathbf{Mg}^{+2}, Al^{+3})_1(\mathbf{Al}^{+3}, Mg^{+2}, Va^0)_2(\mathbf{Va}^0, Mg^{+2})_2(O^{-2})_4$. Its homogeneity range extends to rather close to the Al_2O_3 side and on that side the formula would be $(Al^{+3})_1(Al^{+3}, Va^0)_2(Va^0)_2(O^{-2})_4$, which is identical to a known but metastable modification of alumina called γ-alumina or γ-Al_2O_3. However, it is not an end-member in the model but a solution between two end-members, five parts of AlAlVa and one part of AlVaVa.

The homogeneity range does not at all reach so close to the MgO side and it is not so critical how the state for pure MgO is described. In principle, it might be possible to model that state by introducing vacancies in the first sublattice and gradually deplete it of atoms as the fraction of Mg in the interstitial sublattice grows to unity, yielding the final formula for pure MgO as $(Va)_1(Mg^{+2})_2(Mg^{+2})_2(O^{-2})_4$, which would be identical to the stable form of MgO. However, this has not yet been attempted. Hallstedt's model yields $(Mg^{+2})_1(Mg^{+2})_2(Va^0, Mg^{+2})_2(O^{-2})_4$, which would be a mixture of one part of MgMgMg and one part of MgMgVa.

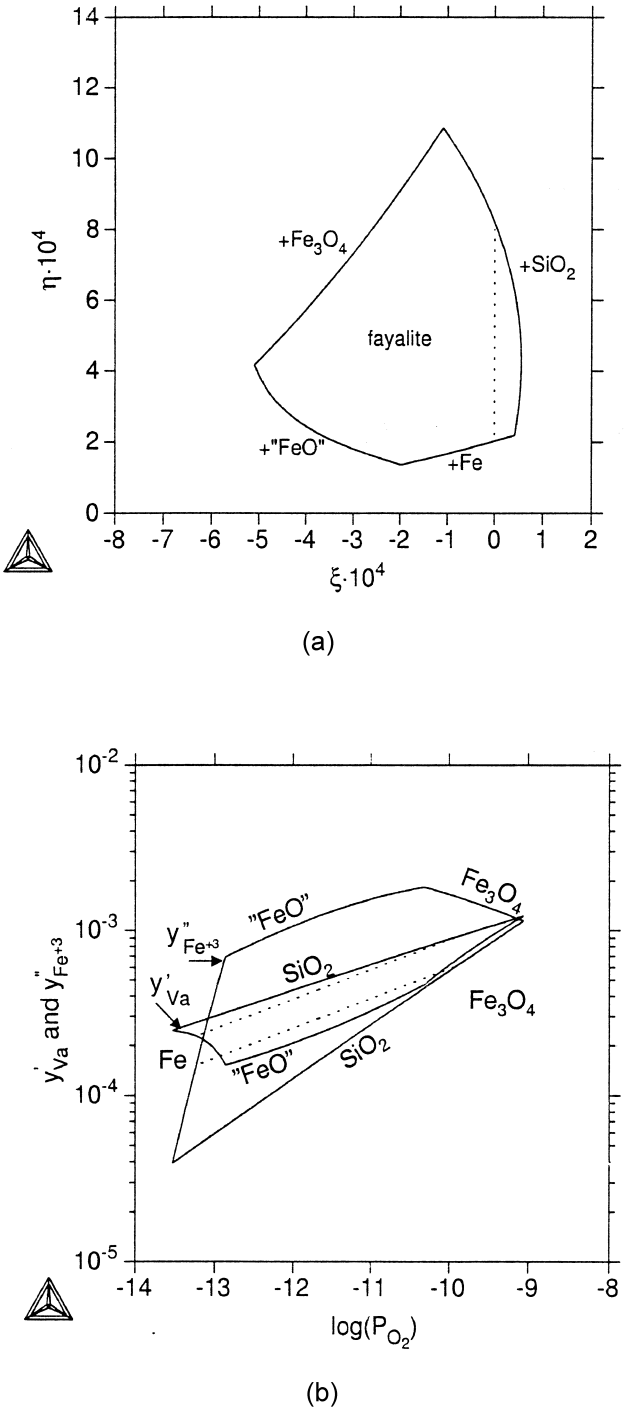

Fig. 3. (A) The calculated deviations from the ideal composition, Fe_2SiO_4, around its field of existence. It is interesting to note that experimental information was limited to the dotted line. (B) The calculated fraction of vacancies in the Fe sublattice and Fe^{+3} in the Si sublattice plotted versus the oxygen pressure. The dotted lines show the variations for a specimen with a close to ideal Fe/Si ratio.

Hallstedt was able to fit the experimental data very well and his calculated phase diagram is shown in Fig. 4A. An illustration of all possible variations in the amounts of various defects would require a four-dimensional picture. However, very few vacancies remain in the second sublat-

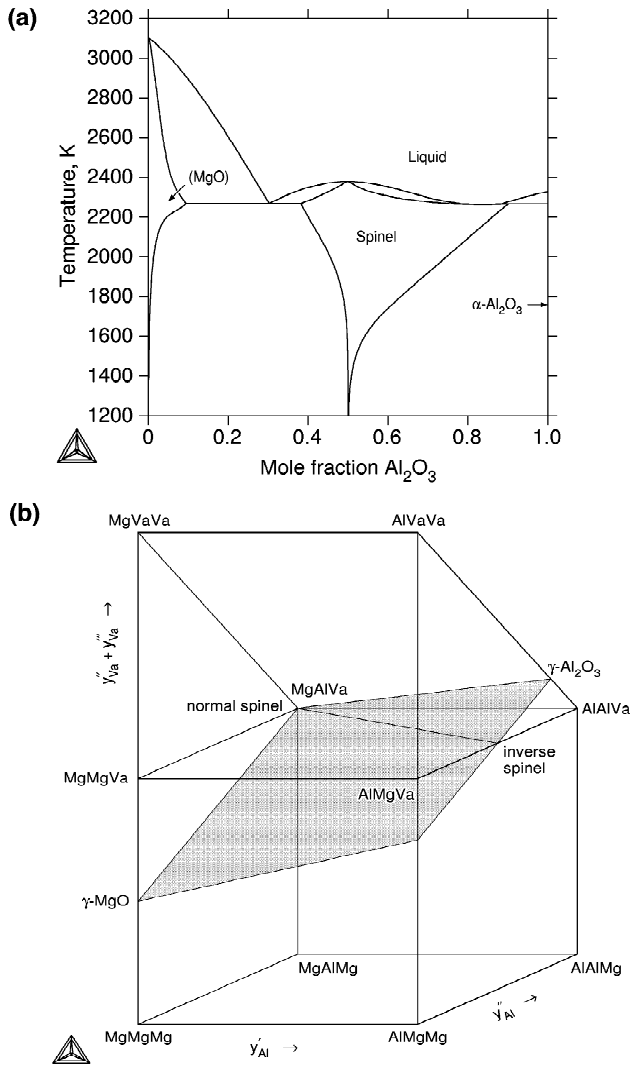

Fig. 4. (A) The calculated MgO–Al_2O_3 phase diagram as optimised by Hallstedt. (B) The compositional space for the spinel phase. The neutral plane is shaded.

tice when they start to be replaced by Mg in the interstitial sublattice, the third one. One can thus give a reasonably representative picture in three dimensions by plotting the total vacancy content on one axis. This is illustrated in Fig. 4B where the neutral plane is shaded. The constitution of the spinel phase extends from the point marked γ-Al_2O_3, moving towards the MgAlVa corner but not quite reaching it when starting to bend and move towards the point marked γ-MgO.

Example 5. Liquidus of an intermetallic phase in the Mg–Sb system with a strong ionisation tendency (reference section 12 in Ref. [2]).

The liquidus of an intermetallic phase is more narrow the more stable the liquid phase is in the same range of composition. This will happen if there is a strong tendency of ionisation in the liquid by charge transfer between the two metals. The Mg-Sb system is an extreme case. It was assessed by Jönsson and Ågren [15] using the compound energy model for melts with an ionisation tendency. Their model for the liquid was $(Mg^{+2})_P(Sb^{-3}, Va^{-Q}, Sb^0)_Q$ and their calculated phase diagram is reproduced in Fig. 5A. It represents most of the experimental data very well.

Fig. 5B shows the calculated tendency of ionisation in the liquid at 1200 K as function of composition. The

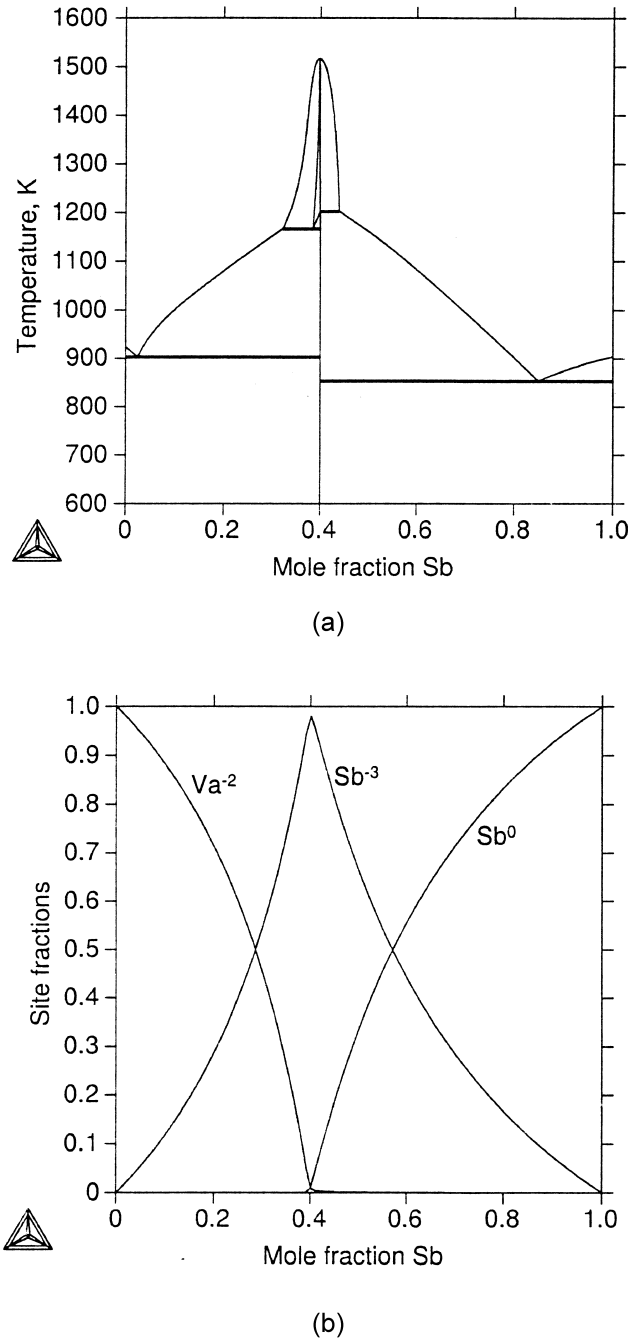

Fig. 5. (A) The calculated Mg–Sb phase diagram as optimised by Jönsson and Ågren. (B) The fraction of the different species on the second sublattice plotted versus the Sb content showing the strong ionisation around $x_{Sb} = 0.4$.

ionisation is very strong in the liquid at the composition of the Mg_3Sb_2 compound.

Example 6. The ionic two-sublattice liquid model applied to oxide melts (reference section 12 in Ref. [2]).

It is of great importance for the steel industry to be able to control the behaviour of slags in order to produce exactly the steel quality they want. The slag used in a BOF (basic oxygen furnace) process can be simplified to consist of CaO–Fe–O–MgO–MnO–SiO_2. The slag would be in equilibrium with a steel melt. To model this situation the thermodynamic descriptions of the slag, the steel and also all the solid oxides within the system, i.e. Ca–Fe–Mg–Mn–O–Si, are needed.

The ionic two-sublattice liquid model [16,17], conforms with the compound energy formalism and is used when there is a tendency for ionisation in the liquid, e.g. liquid oxides and sulphides. The model can describe both the metallic and the slag or matte phase with one set of parameters. It will here be discussed how such a liquid is modelled. Several other examples (2, 3 and 4) describe modelling of solid oxides.

For a normal binary metallic system the model for the liquid is compatible with an ordinary regular solution model and hence evaluations using such a model can be used directly. For instance, the model for Ca–Si–O would yield $(Ca^{+2}, Si^{+4})_P(Va^{-Q})_Q$ for Ca–Si. To model the multicomponent system the Me–O binaries, Ca–O, Fe–O, Mg–O, Mn–O and Si–O, must be evaluated. As an example of Me–O binaries, the Ca–O system was modelled [10] with the formula $(Ca^{+2})_P(O^{-2}, Va^{-Q})_Q$ describing the liquid from pure metal to the corresponding oxide, i.e. CaO. A neutral O species may be added on the second sublattice to describe the liquid all the way to pure oxygen. The Si–O system is a little more complicated since liquid SiO_2 forms a neutral network. It has therefore been modelled [18] $(Si^{+4})_P(O^{-2}, Va^{-Q}, SiO_2)_Q$. The Fe–O system is again more complicated since Fe has two oxidation states, Fe^{+2} and Fe^{+3}. FeO is a basic oxide whereas Fe_2O_3 is amphotere in character, i.e. can act both as an acidic and as a basic oxide. Fe–O was first [9] modelled $(Fe^{+2}, Fe^{+3})_P(O^{-2}, Va^{-Q})_Q$ but later, using the neutral $FeO_{1.5}$ species, emphasising the acid behaviour of Fe_2O_3, the following model was used [19], $(Fe^{+2})_P(O^{-2}, Va^{-Q}, FeO_{1.5})_Q$.

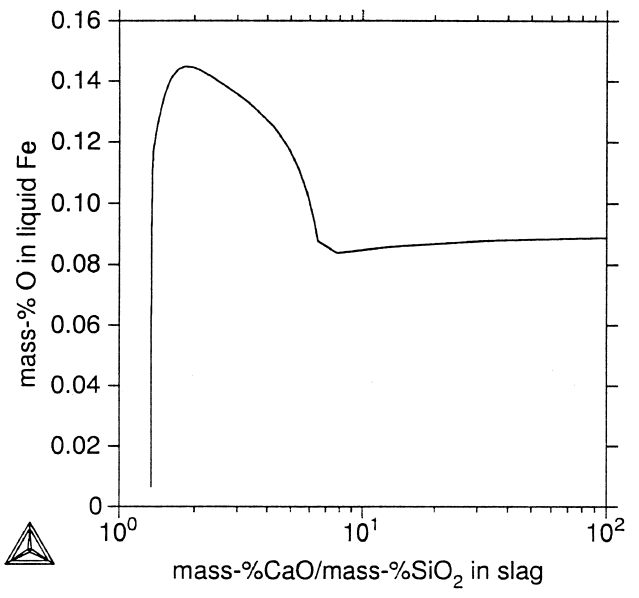

Fig. 6. The basicity (mass pct CaO/mass pct SiO_2) of the slag phase plotted versus the oxygen content in liquid iron at 1873 K. The two liquids are in equilibrium with each other and with different solid oxides — changing with composition.

Using the oxides as components the Ca–O system would be a 'unary' describing CaO. The Fe–O system would be a 'binary' describing FeO–Fe_2O_3. For a system like Ca–Mg–O where the metals have only one valency state the ternary becomes a 'binary', CaO–MgO. The ionic two-sublattice liquid model gives $(Ca^{+2}, Mg^{+2})_P(O^{-2}, Va^{-Q})_Q$. If, however, the interest is the oxide part of the system the vacancies may be excluded from the model. A corresponding system containing Fe, say Ca–Fe–O would of course be an oxide ternary, CaO–FeO–Fe_2O_3. The vacancies should not be excluded from such a system since the FeO–Fe_2O_3 side would be affected.

When a basic oxide such as CaO or MgO is mixed with SiO_2, the slag at $x_{SiO_2} = 1/3$, the orthosilicate composition, consists of almost entirely cations and SiO_4^{-4} anions. When the SiO_2 content is increased further, circular or spherical anions of the kind $Si_3O_9^{-6}$, $Si_4O_{12}^{-8}$ etc will appear. Since the experimental information is not enough to describe parameters for all the occurring species, the model can be simplified by having neutral SiO_2 in combination with SiO_4^{-4} represent all such species. The model for the Ca–Si–O system, would be $(Ca^{+2}, Si^{+4})_P(O^{-2}, SiO_4^{-4}, Va^{-Q}, SiO_2)_Q$, but if only the CaO–$SiO_2$ system was to be described, the species Si^{+4} and Va^{-Q} could be excluded.

Having assessed all the subsystems of the large Ca–Fe–Mg–Mn–O–Si system the model would now be $(Ca^{+2}, Fe^{+2}, Mg^{+2}, Mn^{+2}, Si^{+4})_P(O^{-2}, SiO_4^{-4}, Va^{-Q}, FeO_{1.5}, SiO_2)_Q$. The model contains 17 compounds (end-members), three of which have the SiO_2 composition, $(Si^{+4})_2(O^{-2})_4$, $(Si^{+4})_4(SiO_4^{-4})_4$ and SiO_2. To avoid the first two SiO_2-compounds their Gibbs energies should be given hypothetical high values and not be varied during the optimisation.

When the liquid is liquid metal, e.g. iron modelled as Fe^{+2}, the second sublattice is filled with vacancies with an induced charge of -2. When the liquid is pure Fe_2O_3 or SiO_2 (or any other liquid compound modelled with a neutral species) the number of sites on the first sublattice, P, is zero and therefore its contents and charge are of no importance.

Fig. 6 shows a calculation at 1873 K for a subsystem of the slag discussed above, CaO–Fe–O–SiO_2. The slag

phase is in equilibrium with liquid iron and a solid oxide and the oxygen content in liquid iron is plotted versus the basicity of the slag. The liquid iron and the slag are modelled with the ionic two-sublattice model with one set of parameters [20]. The two liquids are separated by a miscibility gap.

Example 7. Assessment of multi-component systems with high carbo-nitride contents with focus on cemented carbide applications. The use of reciprocal parameters. (reference sections 3 and 9 in Ref. [2]).

Cemented carbides are important cutting tool materials. They consist of 60–90 volume % carbides embedded in a soft matrix phase. The main carbides are WC and TiC; in addition TaC and NbC can be present. The matrix phase is normally Co. Thermodynamic calculations applied to this type of alloys will require a description of the alloy system C–Co–Nb–Ta–Ti–W.

To increase wear resistance cemented carbides can be coated with hard phases. Due to differences in thermal expansion between coating and cemented carbide there is a risk for crack formation in the cemented carbide originating from the coating. For this reason it is important to have a zone in the cemented carbide, below the coating, which has an increased toughness. This can be achieved by creating a nitrogen gradient in the cemented carbide during sintering [21]. For thermodynamic calculations of this specific application, the addition of N to the thermodynamic description of the alloy system C–Co–Nb–Ta–Ti–W is necessary.

The creation of the nitrogen gradient during sintering has been calculated [22,23] with the DICTRA software [24], which uses a full thermodynamic description of the multicomponent system. The agreement of such calculations with experimental information is dependent on the availability of a reliable thermodynamic description of matrix phase and of the carbides, nitrides and carbonitrides of the system. The practical interest is centred on the cubic carbo-nitride (cF8), and some aspects in the modelling of this phase and the evaluation of the model parameters are discussed below. The results are taken from an ongoing project concerning the assessment of Metal–Carbide–Nitride systems.

The cubic carbonitride is described as a C and N rich solution in the fcc structure of the metal. The fcc phase is described by the formula: $(\mathrm{Co, Ti, Ta, Nb, W})_1(\mathrm{C, N, Va})_1$, where Va stands for vacancies. The region of low vacancy content thus describes the properties of the carbo-nitride. The expression for the Gibbs energy of the fcc phase consists of a surface of reference (see Eq. (2) in section 2 in Ref. [2]) which involves 15 end members,

$$G_m = \sum_{\mathrm{Me}} y_{\mathrm{Me}} y_{\mathrm{C}}\, {}^{\mathrm{o}}G_{\mathrm{Me:C}} + \sum_{\mathrm{Me}} y_{\mathrm{Me}} y_{\mathrm{N}}\, {}^{\mathrm{o}}G_{\mathrm{Me:N}} + \sum_{\mathrm{Me}} y_{\mathrm{Me}} y_{\mathrm{Va}}\, {}^{\mathrm{o}}G_{\mathrm{Me:Va}} + {}^{\mathrm{E}}G_m \quad (8)$$

where Me represents Co, Ti, Ta, Nb and W. The Gibbs energy of the end members which have C or N on the second sublattice, ${}^{\mathrm{o}}G^{\mathrm{fcc}}_{\mathrm{Me:C}}$ and ${}^{\mathrm{o}}G^{\mathrm{fcc}}_{\mathrm{Me:N}}$, were determined from experimental or estimated information on the corresponding carbides and nitrides. The properties of the end members with vacancies on the second sublattice are taken from the SGTE pure elements database [25]. The values of the reaction parameters (according to Eq. (7), section 3 of Ref. [2]), ${}^{\mathrm{o}}G_{\mathrm{A,B:C,D}}$, are thus determined from the unary and binary information.

In the present case, the excess term G_m (see Eq. (5), section 2 in Ref. [2]), is composed of terms that have been evaluated from binary, ternary and quaternary experimental information, see for example [26]. The model parameters, which could not be determined by assessing experimental information, were set to zero.

A central quaternary system for the application is the Ti–W–C–N system. In the assessment of the carbonitrides in this system, a problem has been the prediction of a large reciprocal miscibility gap in the fcc phase [27], which is caused by the value of the reaction parameter ${}^{\mathrm{o}}\mathrm{G}_{\mathrm{Ti,W:C,N}}$ (see section 3 in Ref. [2]). This problem was recently discussed in [28]. Since there is experimental evidence in this system indicating that the size of the miscibility gap is overestimated, it was reduced by introducing a reciprocal term: $-y_{\mathrm{Ti}}y_{\mathrm{W}}y_{\mathrm{C}}y_{\mathrm{Va}}({}^{\mathrm{o}}G_{\mathrm{Ti,W:C,N}})^2/z\mathrm{RT}$, to the expression for the excess Gibbs energy. The calculated miscibility gap in the fcc phase is shown in Fig. 7A, which is taken from Ref. [28]. The figure compares the size of the miscibility gap with and without the introduction of the reciprocal term.

Based on the experience from Ti–W–C–N, a reciprocal term was added in the following systems: Nb–W–C–N, Nb–Ta–C–N, Nb–Ti–C–N, Ta–W–C–N, Ta–Ti–C–N, and Ti–W–C–N. Fig. 7B compares the calculated miscibility gaps in a few systems with and without the reciprocal term.

Example 8. The use of estimated information in the assessment of the Ta–N system (reference section 9 in Ref. [2]).

A reliable thermodynamic description of the properties of carbides and nitrides is important for a number of practical applications. The thermodynamic description can be used, together with data on mobilities, as an input to diffusion calculations [24]. This opens a possibility to simulate a number of interesting practical applications, for example precipitation of carbides during solidification, dissolution or precipitation of carbides during heat treatments. The accuracy of the thermodynamic information will affect the predictive ability of the calculations. When calculating equilibria in multicomponent alloys it is important that the relative stability of the various carbides, nitrides and carbonitrides is correctly described. The thermodynamic description of a multicomponent carbonit-

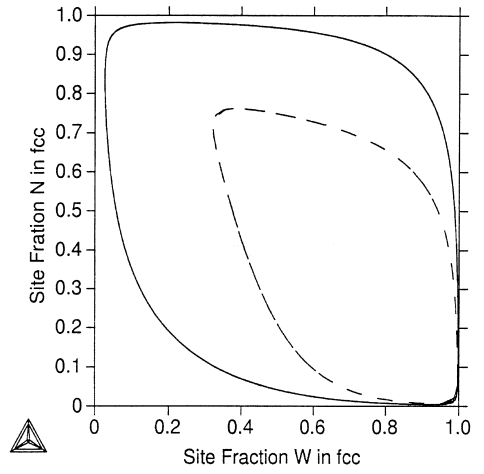

Fig. 7. (A) The calculated miscibility gap in the fcc phase in the Ti–W–C–N system, from Ref. [28]. The dashed line shows the miscibility gap after the introduction of the reciprocal term. The full line shows the calculated miscibility gap when the reciprocal term is zero. (B) Comparison between the calculated miscibility gaps with (dashed line) and without (full line) the reciprocal term in the Ta–Ti–C–N and the Nb–Ti–C–N systems.

ride, using the compound energy model and the CALPHAD approach, is based on an individual assessment of each binary system from experimental information. The experimental information concerning binary nitrides and carbides is however often incomplete or lacking, in particular thermochemical information. When combining a number of binary systems, to form the description of the multicomponent alloy, there is a risk of conflicting data and reassessments of binary systems may be necessary.

To avoid problems in multicomponent alloys a reliable method to estimate lacking information is needed. Different methods can be used to estimate the properties of carbides and nitrides when the experimental information is lacking. A method to estimate the 'compound energies', which is based on comparisons with related carbides/nitrides [29–32] and has been tested in a number of binary assessments [33–35], is used in the example below. The example of the assessment of the Ta–N system [36] shows that the assessment procedure was simplified by the use of estimated parameters.

As described in section 2 in Ref. [2], the expression for the Gibbs energy of a phase ϕ in the binary system Ta–N is given by,

$$G_m^{\phi} = y_N {}^{o}G_{Ta:N}^{\phi} + y_{Va} {}^{o}G_{Ta:Va}^{\phi} + c\,RT(y_N \ln y_N + y_{Va} \ln y_{Va}) + y_N y_{Va} L_{Ta:N,Va}^{\phi}$$

Because $y_{Ta} = 1$, the second term, ${}^{o}G_{Ta:Va}$, represents the Gibbs energy of pure Ta in the state ϕ, and is taken from Ref. [25]. The last term, $L_{Ta:N,Va}$, is optimised from experimental information in the binary Ta–N system. The first term, ${}^{o}G_{Ta:N}$, represents the Gibbs energy of the phase ϕ when all sites are filled with N, which is the same as the stoichiometric nitride in the structure ϕ. In the Ta–N system there are two nitrides with a measured homogeneity range, the hexagonal Ta_2N_x nitride and the cubic δ-TaN_x nitride. The Gibbs energy of the bcc phase, which dissolves low amounts of N and is described by the model $Ta(N, Va)_3$, involves a parameter ${}^{o}G_{Ta:N}^{bcc}$, which represents the Gibbs energy of a hypothetical nitride TaN_3. In the assessment of Ta–N a method proposed by Grimvall and Fernández Guillermet [29–32] for the estimation of entropies of nitrides was used together with experimental or calculated [37] enthalpies of formation to fix the value of ${}^{o}G_{Ta:N}$ for the bcc, fcc and hcp phases. Fig. 8A shows the calculated phase diagram using the estimated ${}^{o}G_{Ta:N}$ values, with the excess term set to zero and together with the assessed liquid phase parameters. As seen by comparing with the final calculation of the Ta–N phase diagram, Fig. 8B, the estimated information gave excellent start points for the assessment.

Example 9. Order–disorder of Ni_3Al treated with an excess term in a two-sublattice model (reference section 7 in Ref. [2]).

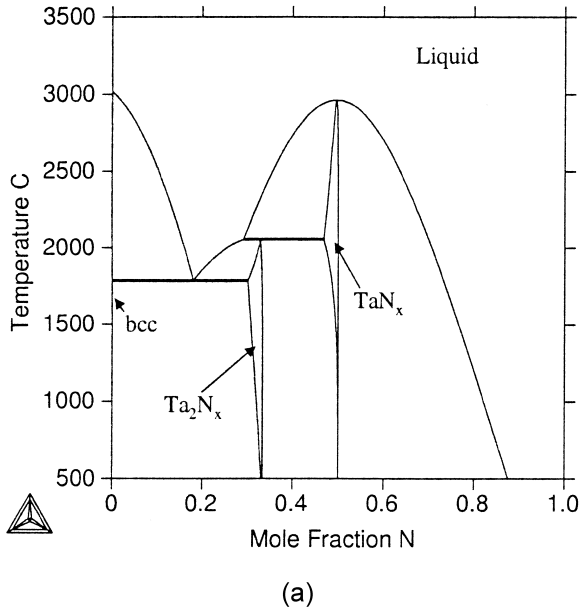

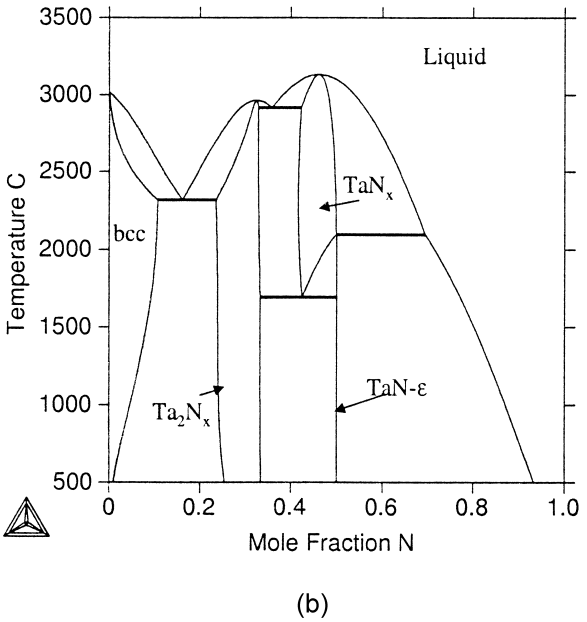

Fig. 8. (A) The calculated Ta–N phase diagram from estimated parameters for the hexagonal Ta_2N_x nitride and the cubic δ-TaN_x nitride and the optimised parameters for the liquid phase. (B) The calculated Ta–N phase diagram according to the assessment in Ref. [36].

Intermetallic phases with sublattices are very common in alloy systems. Most of them are ordered and, although the long range order decreases at high temperatures and there may be large deviations from the stoichiometric composition, they do not lose long range order completely. However, there are cases, above all those with the $L1_2$ structure, where long range order can disappear completely. This can be modelled by standard methods using four sublattices but one could decrease the computation time by using only two sublattices. However, in order to allow the complete loss of long range order it is then necessary to impose some constraints on the parameter values. This was demonstrated by Ansara et al. [38] and applied to the Ni_3Al phase in an assessment of the complete Al–Ni system.

Ni_3Al does not lose its long range order at high temperatures before melting but it does transform to the disordered fcc (A1) phase on the Ni rich side of the system. Ansara et al. were able to describe the whole phase diagram using a single model for the Ni_3Al and fcc phases. It should be mentioned that the stable Al_3Ni phase has a different structure and was modelled as a perfect stoichiometric phase. Of course, it was necessary to check that the common description of the Ni_3Al and fcc phases was such that the possible Al_3Ni phase with the $L1_2$ structure was not predicted to form in competition with the actual Al_3Ni phase (Fig. 9).

Example 10. The role of short range order in Au–Cu. (reference section 13 in Ref. [2]).

In order to model the disordered fcc phase (A1) and the ordered Au_3Cu ($L1_2$), AuCu ($L1_0$) and $AuCu_3$ ($L1_2$) with a single model, it is necessary to consider four sublattices. When using simple bond energy models as well as the basic compound energy model, the phase fields for the three ordered phases are not separated from each other and the experimental phase diagram cannot at all be reproduced. The classical example is Shockley's calculation which predicts that all three should have a common maximum at the 50/50 composition. More satisfactory results have been obtained using the CVM technique which gives an adequate description of the effect of short

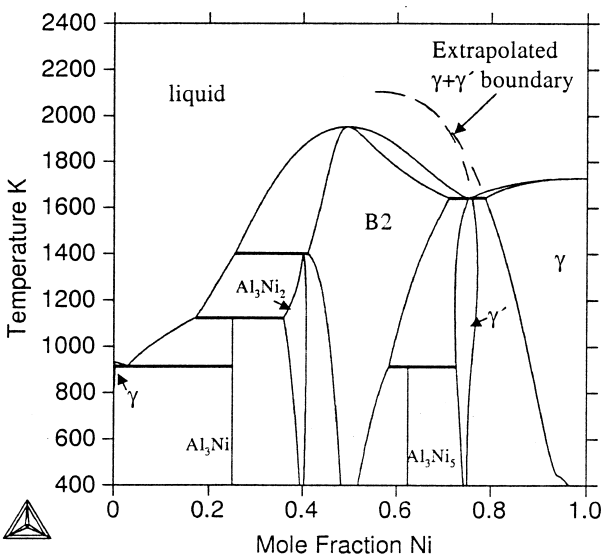

Fig. 9. The calculated Al–Ni phase diagram according to Ref. [38] with the Ni_3Al/fcc phase boundaries extrapolated to very high temperatures to show the metastable, upper point of transition.

range order by considering various kinds of clusters. The short range order in the disordered phase will increase its stability and extend its phase field to lower temperatures and thus separate the ordered regions.

Recently Sundman et al. [39] have shown that already the very crude treatment of short range order by including the so-called reciprocal parameter is sufficient for a satisfactory description of the phase diagram. Fig. 10A reproduces their Au–Cu phase diagram whereas Fig. 10B shows the unrealistic shape obtained when the reciprocal parameter is not included.

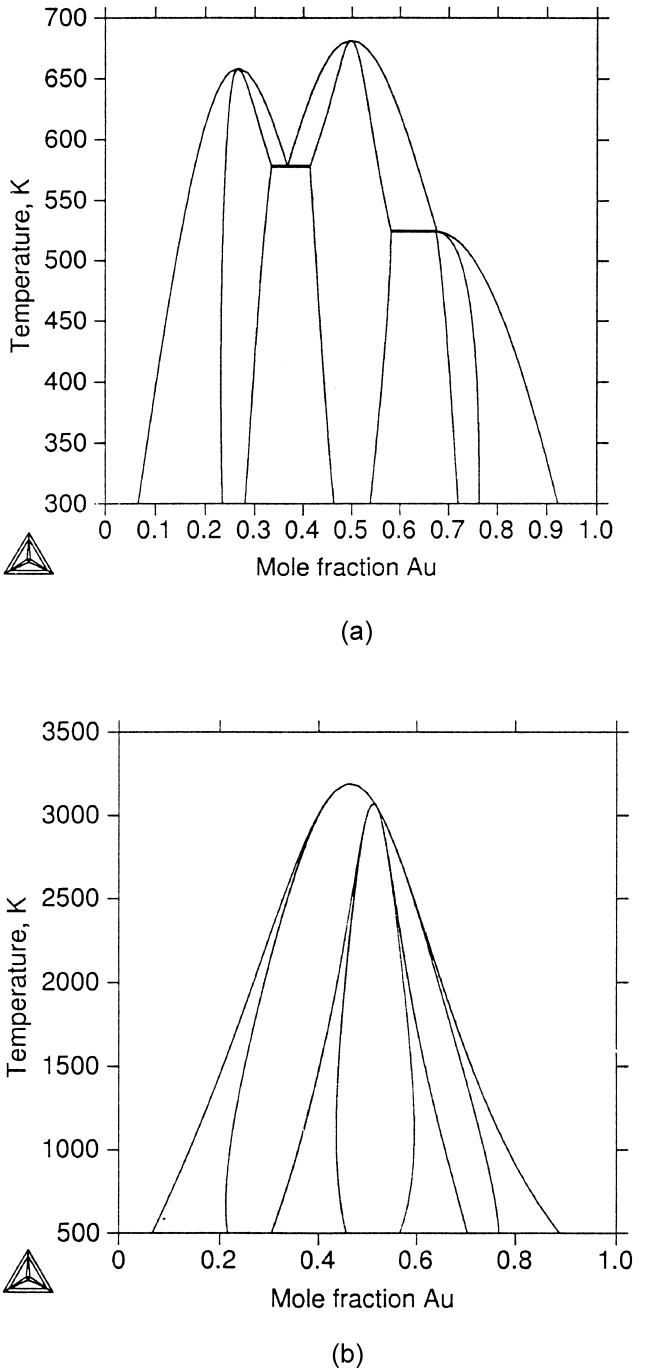

Fig. 10. (A) The calculated Au–Cu phase diagram assessed by Sundman et al. (B) The calculated Au–Cu phase diagram when the reciprocal parameter is omitted.

Example 11. Semiconducting properties and non-stoichiometry of CdTe in a five-sublattice model (reference sections 5, 6 and 11 in Ref. [2]).

The III–V semiconductors have important technical applications. An important aspect is that their electrical properties can be varied continuously by gradually adding another III or V metal. Rational production of these materials can be supported by detailed knowledge of the stability relative to the liquid phase and of the deviation from stoichiometry as a function of the vapour pressure of Cd, for instance. Thus, it is highly desirable to have an adequate description of the thermodynamic properties of the multicomponent III–V compounds but that would require that one takes due account of the existence of different sublattices for the III and V metals and the presence of anti-site atoms. It is thus necessary to use a sublattice model and preferably one which fits into the compound energy formalism.

In order to describe the electrical properties it is essential to consider the presence of free electrons and electron holes as well as ionised atoms even though those point defects have a negligible influence on the thermodynamic properties. This was done by Chen et al. [40] who applied a compound energy model to the Cd–Te system choosing four sublattices, one each for the III and V metals and one each for the electrons and holes.The contents of the defects are very low and a dilute solution approximation would be adequate. However, it is necessary to use a sublattice model in order to model more than one III or V metal.

Several definitions of the formula unit were tried and, finally, following a proposal by Chern et al. [41], interstitial Cd and Cd^{+2} were introduced in order to explain low temperature data for the semiconducting properties, i.e. a total of five sublattices were used: $(Cd, Va, Va^{-2}, Te)_1(Te, Va, Va^{+2}, Cd)_1(Va, Cd, Cd^{+2})_1(Va, e^{-})_1(Va, h^{+})_1$. The result is demonstrated by the calculated diagram in Fig. 11A, showing the various defect contents at a temperature of 900°C as function of the Cd vapour pressure. At room temperature the equilibrium contents of all the charged defects are very low and positive and negative defects could thus annihilate each other on cooling. The dashed curve shows the final content of electrons if their annihilation only occurs by reaction with the holes. The dotted curve was obtained if the electrons are also annihilated by combination with Cd^{+2} to form neutral Cd. It now turns out that the experimental data falls even lower, indicating that either some electrons are annihilated by reaction with the positive vacancies or the amount of Cd^{+2} was a little higher than according to the assessment by Chen et al.

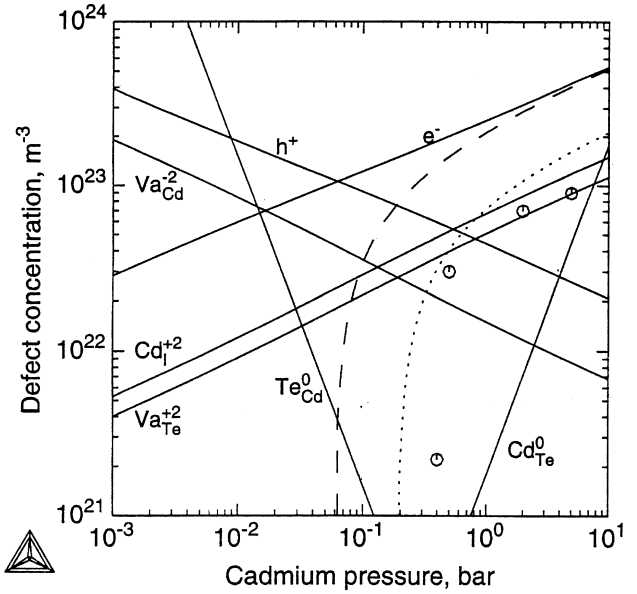

(a)

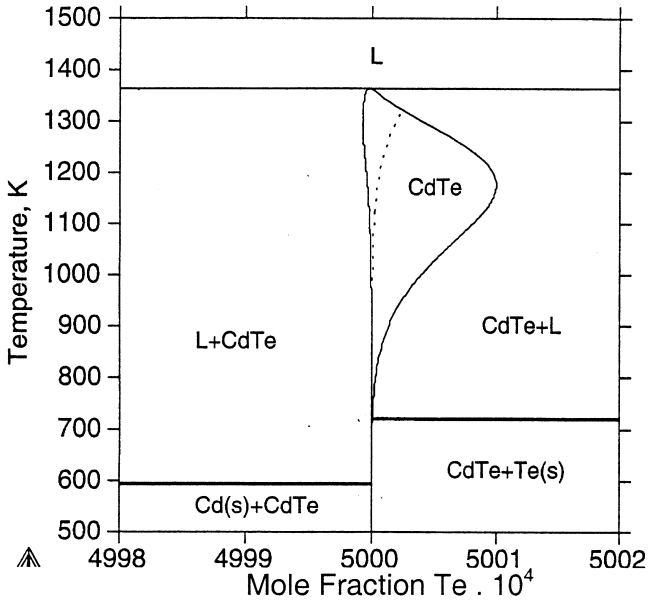

(b)

Fig. 11. (A) The calculated defect contents in Cd–Te at 900°C as a function of the Cd vapour pressure. (B) The calculated phase diagram for the Cd–Te system. The central part of the diagram with the one phase field for the semiconducting phase CdTe is shown. The dotted line shows where the vapour pressure of Cd and Te are equal.

That could easily have been be accomplished by decreasing Va^{+2} by the same amount.

The choice of divalency, for the vacancies and the Cd ions, affects the slopes of the lines for electrons and holes in Fig. 11A and was supported by experimental data on the slopes of those lines.

Fig. 11B shows the central part of the calculated phase diagram with the one-phase field for the semiconducting phase, CdTe. The dotted line shows where the vapour pressures of Cd and Te are equal and may be regarded as the sublimation line. The possibility to calculate the vapour pressures within this region can be utilised for controlling the defect contents in the production of these materials.

Acknowledgements

We would like to express our gratitude to Prof. Mats Hillert who invited us to write this paper accompanying his paper on the Compound Energy Formalism, and for help received during the work. We would also like to thank Tekn Lic Alexandra Kusoffsky, Dr Bengt Hallstedt, Dr Qing Chen, Docent Staffan Hertzman, Prof. I. Ansara for calculating or supplying some of the figures.

References

[1] M. Hillert, L.-I. Staffansson, Acta Chem. Scand. 24 (1970) 3618.
[2] M. Hillert, J. Alloys Comp. 320 (2001) 161–176.
[3] H. Hänninen, S. Hertzman, J. Romu (Eds.), High Nitrogen Steels 1998. Proceeding of the 5th International Conference on High Nitrogen Steels, Espoo, Finland and Stockholm Sweden, May 1998, Trans Tech Publications Ltd., Switzerland, 1999.
[4] L. Kaufman, H. Bernstein, Computer Calculation of Phase Diagrams, Academic Press, New York, 1970.
[5] N. Saunders, A.P. Miodownik, in: CALPHAD Calculation of Phase Diagrams, Pergamon Materials Series, Vol. 1, 1998, pp. 332–344.
[6] S. Hertzman, Scand. J. Metallurgy 24 (1995) 140–146.
[7] K. Frisk, in [3], p. 95.
[8] S. Hertzman, P.J. Ferreira, B. Brolund, Metall. Mat. Trans. 28A (1997) 297.
[9] B. Sundman, J. Phase Equilibria 12 (1) (1991) 127–140.
[10] M. Hillert, M. Selleby, B. Sundman, Metall. Trans. A 21A (1990) 2759–2776.
[11] T.I. Barry, F.P. Glasser, NPL Rep. DMA(A) 169 (1988).
[12] M. Hillert, M. Selleby, B. Sundman, Phys. Chem. Minerals 23 (1996) 387.
[13] A. Nakamura, H. Schmalzried, Phys. Chem. Minerals 10 (1983) 27.
[14] B. Hallstedt, J. Am. Ceram. Soc. 75 (1992) 1497.
[15] B. Jönsson, J. Ågren, Metall. Trans. 18A (1987) 1395.
[16] M. Hillert, B. Jansson, B. Sundman, J. Ågren, Metall. Trans. A 16A (1985) 261–266.
[17] B. Sundman, Calphad 15 (1991) 109–119.
[18] B. Hallstedt, J. Phase Eq. 14 (1993) 662–675.
[19] M. Selleby, B. Sundman, Calphad 298 (1996) 381–392.
[20] M. Selleby, Metall. Mat. Trans. B 28B (1997) 577–596.
[21] H. Suzuki, K. Hayashi, Y. Taniguchi, Trans. Japan Inst. Metals 22 (11) (1981) 758–764.
[22] M. Ekroth, J. Ågren, in: M. Koiwa, K. Otsuka, T. Miyazaki (Eds.), Proc. Int. Conf. Solid–Solid Phase Transformations '99 (JIMIC-3), The Japan Institute of Metals, 1999, pp. 1413.16.
[23] M. Ekroth, J. Ågren, to be presented at Sintering 1999, The Second International Conference on Science, Technology and Applications of Sintering, Nov 1–3 1999, Pennsylvania, USA.
[24] J.O. Andersson, L. Höglund, B. Jönsson, J. Ågren, in: G.R. Purdy (Ed.), Fundamentals and Applications of Ternary Diffusion, Pergamon Press, New York, NY, 1990, pp. 153–163.
[25] A.T. Dinsdale, Calphad 15 (1991) 317–425.

[26] W. Huang, Z. Metallkd. 88 (1997) 63.
[27] S. Jonsson, Z. Metallkd. 87 (1996) 788–795.
[28] M. Ekroth, K. Frisk, B. Jansson, L.D. Dumitrescu, Metallurgical and Materials Transactions 31 B (2000) 615–619.
[29] A. Fernández Guillermet, G. Grimvall, Phys. Rev. B 40 (1989) 10582–10593.
[30] A. Fernández Guillermet, G. Grimvall, J. Phys. Chem. Solids 53 (1992) 105–125.
[31] A. Fernández Guillermet, J. Häglund, G. Grimvall, Phys. Rev. B 45 (1992) 11557–11567.
[32] A. Fernández Guillermet, J. Häglund, G. Grimvall, Phys. Rev. B 48 (1993) 11673–11684.
[33] A. Fernández Guillermet, K. Frisk, Int. J. Thermophys. 12 (1991) 417–431.
[34] A. Fernández Guillermet, S. Jonsson, Z. Metallkd. 83 (1992) 21–31.
[35] A. Fernández Guillermet, S. Jonsson, Z. Metallkd. 84 (1993) 106–117.
[36] K. Frisk, J. Alloys Comp. 278 (1998) 216–226.
[37] F.R. de Boer, R. Boom, W.C. Mattens, A.R. Miedema, A.K. Niessen, Cohesion in Metals, Transition Metal Alloys, North Holland, Amsterdam, 1988.
[38] I. Ansara, N. Dupin, H.L. Lukas, B. Sundman, J. Alloys Comp. 247 (1997) 20.
[39] B. Sundman, S.G. Fries, W.A. Oates, Calphad 22 (1998) 335.
[40] Q. Chen, M. Hillert, B. Sundman, W.A. Oates, S.G. Fries, R. Schmidt-Fetzer, J. Electronic Materials 27 (1998) 961.
[41] S.S.S. Chern, H.R. Vydyanath, F.A. Kroger, J. Solid State Chem. 14 (1975) 33.